Available online at www.sciencedirect.com
SCIENCE DIRECT
Journal of Power Sources 156 (2006) 414–423
JOURNAL OF POWER SOURCES
www.elsevier.com/locate/jpowsour

Parametric model of an intermediate temperature PEMFC

Denver Cheddie [1], Norman Munroe *

Mechanical and Materials Engineering, CEAS 2441, Florida International University, 10555 W Flagler Street, Miami, FL 33174, USA

Received 12 May 2005; accepted 3 June 2005
Available online 1 August 2005

Abstract

Proton exchange membrane fuel cells operating with Nafion® membranes have encountered numerous problems associated with water management and CO poisoning because of their low temperature of operation. Higher temperature membranes have been investigated, one such membrane being polybenzimidazole (PBI). This paper presents a parametric model, which predicts the polarization performance of an intermediate temperature proton exchange membrane fuel cell (PEMFC). It also investigates the effects of porous media characteristics on fuel cell performance. Results show that for intermediate temperature fuel cells, mass limitation effects are absent as long as the catalyst regions are sufficiently permeable. It is predicted that the greatest scope for improving PBI PEMFC performance is increasing the membrane conductivity and improving the catalyst performance, as it interfaces with the PBI membrane.

Keywords: Fuel cell; Modeling; PBI; Intermediate temperature

1. Introduction

The proton exchange membrane fuel cell (PEMFC) has long been considered a prime candidate for future energy systems. However, a number of debilitating factors—low electrode kinetics, catalyst poisoning, and membrane materials limitations—have hindered its development.

The Nafion® membrane typically used in low-temperature PEMFCs requires critical water management for sustained operation. As a result, the fuel cell is operated below 90 °C. Proper water management is necessary to simultaneously prevent dehydration of the membrane and flooding of the electrodes. This critical water management requirement makes Nafion® unsuitable for applications with variable loading conditions, such as automotive applications.

At low temperatures, carbon monoxide (CO) poisoning of the platinum (Pt) catalyst is also a problem. Traces of CO, present in the hydrogen feed, are preferentially adsorbed on catalyst sites resulting in reduced efficiency and possible permanent poisoning of the catalyst.

One solution to these problems is operating the PEMFC at intermediate temperatures (150–200 °C). At such temperatures, CO poisoning becomes less prominent, electrode kinetics are faster, and water would exist primarily in the vapor phase precluding problems associated with water management and mass transport limitations. However, since Nafion® requires a high water content to maintain proton conductivity, it is very ineffective at temperatures above the boiling point of water. Therefore, alternative membranes, which maintain mechanical strength and chemical stability at elevated temperatures, are needed.

One such membrane is polybenzimidazole (PBI). PBI has the advantage of being lightweight as well as stable at higher temperatures (150–200 °C), and it attains proton conductivity when doped with phosphoric or sulfuric acid [1–12]. Protons are transported through the solid matrix; so, its conductivity is less dependent on water content than Nafion®. Proton conduction in PBI may be based on the Grotthuss (proton hopping) mechanism, as suggested by

* Corresponding author. Tel.: +1 305 348 3556; fax: +1 305 348 6142.
E-mail addresses: dched002@fiu.edu (D. Cheddie), munroen@fiu.edu (N. Munroe).
[1] Tel.: +1 786 877 9235, fax: +1 305 348 6142.

0378-7753/$ – see front matter © 2005 Published by Elsevier B.V.
doi:10.1016/j.jpowsour.2005.06.010

Nomenclature

a	effective surface area
c	specific heat capacity
d	average diameter of spherical particles
D_m	effective gas diffusivity
D_T	effective thermal diffusivity
E	potential
f	weight fraction of Pt in Pt/C
F	Faraday constant (96,485 C mol^{-1})
i	current density
i_0	exchange current density
j	reaction rate
k	thermal conductivity
k_p	permeability
l	thickness
m	mass fraction, mass loading
M	molar mass
P	pressure
R	universal gas constant (8.3143 J mol^{-1} K^{-1})
S	source, entropy
T	temperature
u	mass-averaged Darcy velocity

Greek letters

α	thermal diffusivity, charge transfer coefficient
ε	porosity
γ	concentration parameter
φ	electrical or ionic potential
ν	kinematic viscosity
ρ	mass density
σ	electrical or ionic conductivity

Bouchet et al. [2,3]. PBI membrane thicknesses are lower than Nafion® because of its higher mechanical strength. A reduction in membrane thickness leads to lower ionic resistance, since resistance is proportional to thickness. In addition, PBI has a lower permeability to hydrogen and methanol than Nafion®, resulting in less crossover of fuel at elevated temperatures.

PBI's conductivity can be further enhanced by alloying with inorganic composites. Several studies have been conducted on the feasibility of using PBI and its composites as membranes in PEMFCs (Ref. [4] and references therein). Composites of PBI have been developed with sulfonated polysulfones (SPSF) [5]; zirconium phosphate (ZrP), phosphotungstic acid (PWA), silicotungstic acid (SiWA) [6]; inorganic phosphomolybdic acid (PMo_{12}) [7]; imidazole and 1-methyl imidazole (Me–Im) [8]; silicotungstic acid and silica [9].

The conductivity of PBI and its composites reportedly depend on the temperature, humidity, doping level of acid treatment, and method of preparation of the membrane. The conductivity of PBI treated with phosphoric acid ranges from 0.2 to 6.8 S m^{-1} [6,9–12]. Doped with sulfuric acid, the conductivity ranges from 5 to 6 S m^{-1} [13,14]. KOH-doped PBI has been reported to have an ionic conductivity of 9 S m^{-1} [13]. Among the composites of PBI, one with 0.15 wt.% ZrP has exhibited a conductivity of 9.6 S m^{-1} [6]. The conductivity of Nafion® for fully humidified membrane conditions is 17 S m^{-1} [15,16]. So, it is evident that PBI-based membranes have relatively lower conductivities than Nafion®. However, since PBI's permissible membrane thickness is less than Nafion®, its ionic resistance is of the same order of magnitude. Table 1 compares typical values of conductivity and membrane thickness for PBI-based membranes and Nafion®. For a given cross-sectional area, the ionic resistances of PBI and Nafion® are in the same order of magnitude.

Table 1
Comparison of PBI and Nafion®

	σ (S m^{-1})	l_m (μm)	Total resistance (Ω cm^2)
PBI	1–9	40–80	0.044–0.800
Nafion®	17	230	0.135

Much work has been done in PEMFC modeling, over the past 15 years, on PEMFCs using Nafion® membranes, i.e. low-temperature PEMFCs [17]. Although intermediate temperature membranes have been investigated for use in PEMFCs, to date, no mathematical model has been published for any intermediate temperature PEMFC. This paper presents a mathematical model of a PEMFC working with a PBI membrane, or a PBI fuel cell (PBIFC). The model is one-dimensional, steady state and non-isothermal. It attempts to simulate the experimental data presented by Wang et al. [18], and also to determine the optimum performance of a PBIFC. Most papers, presenting parametric models, focus on operating conditions. This paper focuses on geometric factors such as porous media characteristics, and membrane and catalyst properties.

2. Model development

2.1. Assumptions

For intermediate temperature fuel cells, water is expected to exist only in the vapor phase, therefore, single-phase assumptions apply. The gas mixtures are assumed to behave ideally. The porous media and catalyst regions are assumed to be isotropic and macro-homogeneous, and the membrane is assumed to be impermeable to gas flow. It is assumed that gases are supplied to the fuel cell at a sufficiently high rate, so that there is little variation in fluid properties along the gas channels. We also neglect rib effects. Using scaling arguments, we expect the most significant variations in transport properties to occur in the direction perpendicular to the membrane electrode assembly (MEA) cross-section. Thus, a one-dimensional treatment of the MEA is adopted.

2.2. Governing equations

The following conservation equations govern the phenomena. The Darcy velocity, u, the source term, S, the temperature, T, and the current densities, i are volume-averaged over the entire porous media (solid and fluid regions). The pressure, P, and density, ρ are volume-averaged over the void region. The phase potentials, φ, are volume-averaged over their respective phases (solid and electrolyte phases).

$$\nabla \cdot (\rho u) = S_{\mathrm{m}} \tag{1}$$

$$S_{\mathrm{m}} = \sum S_i \tag{2}$$

The continuity Eq. (1) has a non-zero term on the RHS, which represents solid–fluid phase change in the catalyst layers. For a PBI membrane, H^+ ions are transported across the membrane in a solid state. So, there is a loss of fluid mass at the anode catalyst layer and a gain in fluid mass at the cathode catalyst layer. Total mass is always conserved at every point, and overall fluid mass in conserved since the H^+, formed at the anode, re-converts to fluid mass at the cathode. Across the membrane, the velocity is zero.

For porous media in fuel cells, the momentum equation scales to Darcy's law. All other terms (inertia, body and viscous terms) are negligible.

$$\nabla P = -\frac{\rho v}{k_{\mathrm{p}}} u \tag{3}$$

Considering that a non-conservative form of the continuity equation is used, the species equations must be re-derived. Conservation of individual species, i, is given by,

$$\nabla \cdot (\rho_i u) = \nabla \cdot (\rho m_i u) = \nabla \cdot (\rho \varepsilon D_{\mathrm{m}} \nabla m_i) + S_i \tag{4}$$

Expanding the LHS and combing with the continuity equation,

$$m_i \nabla \cdot (\rho u) + \rho u \cdot \nabla(m_i) = \nabla \cdot (\rho \varepsilon D_{\mathrm{m}} \nabla m_i) + S_i \tag{5}$$

$$\rho u \cdot \nabla m_i = \nabla \cdot (\rho \varepsilon D_{\mathrm{m}} \nabla m_i) + S_i - m_i S_{\mathrm{m}} \tag{6}$$

The last term on the RHS does not normally appear in the species equation (actually, it is normally zero). However, for this case, where a non-conservative continuity equation is used, it must be included. If Eq. (6) is summed for all species and combined with Eq. (2), both sides of the equation become zero.

The energy equation accounts for convection, conduction and heat generation due to ohmic or Joule heating, as well as heat of reaction.

$$\rho c u \cdot \nabla T = \rho c \nabla \cdot (D_{\mathrm{T}} \nabla T) + S_{\mathrm{T}} \tag{7}$$

$$S_{\mathrm{T}} = S_{\mathrm{ohm}} + S_{\mathrm{rxn}} \tag{8}$$

The charge-conservation equations in the electrolyte and solid phases are given by,

$$\nabla \cdot i_{\mathrm{s}} = \nabla \cdot (-\sigma_{\mathrm{s}}^{\mathrm{eff}} \nabla \phi_{\mathrm{s}}) = -j \tag{9}$$

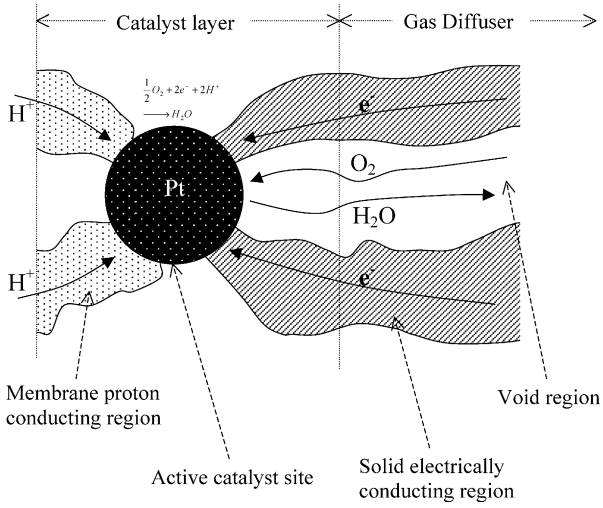

Fig. 1. Schematic of a catalyst site.

$$\nabla \cdot i_{\mathrm{e}} = \nabla \cdot (-\sigma_{\mathrm{e}}^{\mathrm{eff}} \nabla \phi_{\mathrm{e}}) = j \tag{10}$$

$$j = a i_0^{\mathrm{ref}} \left(\frac{p_{\mathrm{reactant}}}{p_{\mathrm{ref}}} \right)^{\gamma_{\mathrm{reactant}}} \left\{ \exp\left[\frac{\alpha F}{RT} (\phi_{\mathrm{s}} - \phi_{\mathrm{e}}) \right] - \exp\left[-\frac{\alpha F}{RT} (\phi_{\mathrm{s}} - \phi_{\mathrm{e}}) \right] \right\} \tag{11}$$

The Butler–Volmer Eq. (11) states that the rate of charge transfer is driven by the difference in potential between the two respective phases, and is affected by the concentration of reactants at the catalyst sites. The reaction rate, j, defines the rate of transfer of solid-state current to electrolyte phase current in the anode catalyst layer, and vice versa in the cathode catalyst layer. Fig. 1 shows a schematic of the catalyst site illustrating the charge transfers. This concept of two phase potential and current flow, often overlooked by most fuel cell modelers, is critical to fully analyze the fuel cell.

The exchange current density, i_0, is defined in terms of the active catalyst surface area. The effective surface area, a, is defined as the ratio of the total active catalyst surface area to the total catalyst region volume. This way the reaction rate is volume-averaged over the entire solid and void phases.

2.3. Source terms

The source terms are given in terms of the reaction rates in each catalyst layer.

$$S_{\mathrm{O_2}} = j \frac{M_{\mathrm{O_2}}}{4F} \tag{12}$$

$$S_{\mathrm{H_2O}} = -j \frac{M_{\mathrm{H_2O}}}{2F} \tag{13}$$

$$S_{\mathrm{H_2}} = j \frac{M_{\mathrm{H_2}}}{2F} \tag{14}$$

$$S_{\text{rxn}} = -j\left(\phi_{\text{e}} - \phi_{\text{s}} - \frac{T\Delta S}{nF}\right) \tag{15}$$

$$S_{\text{ohm}} = \frac{i_{\text{s}}^2}{\sigma_{\text{s}}^{\text{eff}}} + \frac{i_{\text{e}}^2}{\sigma_{\text{e}}^{\text{eff}}} \tag{16}$$

There is no electrolyte current in the diffuser regions, where the second term in the RHS of Eq. (16) is zero. Similarly there is no solid-state current in the membrane, since the membrane is impermeable to electron flow. Both phase currents are present in each catalyst layer.

2.4. Porous media correlations

The following correlations are used to correct the plain media properties for porous media. The Rumpf and Gupte correlation [19,20] is used for permeability. This pertains to a packed bed of spherical particles of average diameter, d.

$$k_{\text{p}} = \frac{\varepsilon^{5.5} d^2}{5.6} \tag{17}$$

The geometric average of the solid and fluid conductivity is used to determine the effective thermal conductivity [19,21].

$$\frac{k_{\text{e}}}{k_{\text{f}}} = \left(\frac{k_{\text{s}}}{k_{\text{f}}}\right)^{1-\varepsilon} \tag{18}$$

The dispersion diffusivity is given by the following relationship, valid for low Peclet number flows [19,22]:

$$\frac{D^{\text{d}}}{\alpha_{\text{f}}} = 3(1-\varepsilon)\left(\frac{\frac{k_{\text{s}}}{k_{\text{f}}} - 1}{\frac{k_{\text{s}}}{k_{\text{f}}} + 2}\right) \tag{19}$$

The total effective thermal diffusivity is given as [19],

$$\frac{D_{\text{T}}}{\alpha_{\text{f}}} = \frac{k_{\text{e}}}{k_{\text{f}}} + \frac{\varepsilon D^{\text{d}}}{\alpha_{\text{f}}} \tag{20}$$

This value depends on solid and fluid properties and compositions, as well as porous media characteristics.

The effective gas diffusivity is related to the plain media diffusivity as follows [19,23],

$$\frac{D_{\text{m}}}{D_{\text{mf}}} = \frac{2\varepsilon}{3-\varepsilon} \tag{21}$$

The electrical and ionic conductivities are corrected for porous media using the Bruggemann correlation [24], where $\varepsilon_{\text{phase}}$ is the volume fraction occupied by the phase through which the respective current flows.

$$\sigma^{\text{eff}} = \sigma\varepsilon_{\text{phase}}^{1.5} \tag{22}$$

The gas mixture density is found from the ideal gas law:

$$\rho = \frac{P}{RT}\left(\sum \frac{m_i}{M_i}\right)^{-1} \tag{23}$$

All other fluid properties, heat capacity, kinematic viscosity, thermal conductivity and thermal diffusivity are mass-averaged for the gas mixture. The plain media gas pair diffusivity is assumed constant at a given temperature and pressure, and independent of composition.

2.5. Boundary conditions

The unified (single domain) approach is used in this model. Thus, boundary conditions are required at the ends of the domain, i.e. at the anode gas channel/gas diffuser interface ($x = 0$, boundary 1) and the cathode gas channel/gas diffuser interface ($x = 0.7$ mm, boundary 2). All state properties and fluxes are continuous at all interfaces.

In the experimental set up of Wang et al. [18], the cell is run at 150 °C and 1 atm, and supply gases are humidified at 28 °C. Thus, the total gas pressure at boundaries 1 and 2 are equal to the respective supply gas pressures, i.e. $P_0 = 101{,}300$ Pa. The temperature at both boundaries is equal to the respective supply gas temperature, i.e. $T_0 = 423$ K. The partial pressure of water vapor is equal to the vapor pressure at 28 °C, which is 0.03782 bar. Thus, the mass fraction of hydrogen at boundary 1 is 0.741, while the mass fraction of oxygen at boundary 2 is 0.979. This is the mass fraction of oxygen when pure oxygen is used as oxidant rather than air. Since there is no flux of hydrogen and oxygen across the membrane, the concentration gradients of each are set to zero at the interfaces of the membrane and the respective catalyst layers.

The solid phase potential is arbitrarily set to zero as a reference at boundary 1, and is set to $E_{\text{cell}} - E_{\text{rev}}$ at boundary 2, where E_{cell} is the desired cell potential and $E_{\text{rev}} = 1.154$ V is the reversible cell potential at 423 K and 1 atm. The solid potential gradient is set to zero are both catalyst layer/membrane interfaces, since there exists no solid phase current in the membrane. The electrolyte phase potential only exists in the catalyst layers and the membrane. Since there is no electrolyte current in the diffuser regions, the electrolyte potential gradient is set to zero are both catalyst layer/diffuser region interfaces.

2.6. Catalyst layer calculations

In Wang et al. [18], E-TEK electrodes with a Pt loading of 0.5 mg cm^{-2} were used at the anode. For the cathode, a homemade electrode was used, where Pt was sputtered on the commercial electrodes to enhance its activity. The total catalyst loading at the cathode was 2 mg cm^{-2}. Although not reported, the catalyst region usually consists of 30 wt.% Pt/C ($f = 0.3$). Since this paper is interested in the effect of porous media characteristics on fuel cell performance, it is necessary to perform catalyst region calculations.

The catalyst region is a fused layer between the membrane and the electrode sputtered with catalyst particles. In this region, there exists membrane phase, diffuser solid and void regions, as well as catalyst particles. There must be adequate physical contact among all the phases for effective electrochemistry (see Fig. 1). The catalyst region consists of the

following regions in the respective proportions:

membrane phase: $\varepsilon_{m,c}$;
diffuser solid region: $(1-\varepsilon_{m,c})\,(1-\varepsilon^{(d)})$;
diffuser void region:$(1-\varepsilon_{m,c})\,(\varepsilon^{(d)}) - m_o/\rho_o\, l_c$;
Pt/C catalyst particles: $m_o/\rho_o\, l_c$.

where m_o and ρ_o are the average catalyst particle mass loading per MEA cross-section and density, respectively. If m_{Pt} is the mass loading of Pt per MEA cross-section, and f is the fraction of Pt in the Pt/C particles, then

$$m_O = \frac{m_{Pt}}{f} \tag{24}$$

$$\rho_O = \left(\frac{f}{\rho_{Pt}} + \frac{1-f}{\rho_C}\right)^{-1} \tag{25}$$

Thus, the porosity of the catalyst region can be determined in terms of the porosity of gas diffusion region and the catalyst packing properties.

$$\varepsilon^{(c)} = \varepsilon^{(d)}(1-\varepsilon_{m,c}) - \frac{m_{Pt}}{l_c\, f}\left(\frac{f}{\rho_{Pt}} + \frac{1-f}{\rho_C}\right) \tag{26}$$

It can also be shown that the effective Pt surface area,

$$a = \frac{6 m_{Pt}}{l_c\, \rho_{Pt}\, d_{Pt}} \tag{27}$$

The diameter of the Pt particles is typically 20 Å [25]. So, the effective surface area can be increased either by increasing the catalyst mass loading or decreasing the mean catalyst particle size.

Because the Pt loading is different at the anode than at the cathode, the f value would also be different. It can be shown that at the cathode, the f value is given as,

$$f_c = \frac{m_{Pt,c}}{m_{Pt,c} + m_{Pt,a}\left(\frac{1-f_a}{f_a}\right)} \tag{28}$$

3. Results and discussion

The governing equations are solved using FEMLAB® 3.0. The domain is divided into 768 finite elements—288 in each gas diffuser sub-domain, 48 in each catalyst layer, and 96 in the membrane. A finite-element method is used to solve the system of coupled partial differential equations.

Tables 2–4 give a list of numerical values used in the computations. This will be called the base case—the same operating and geometric conditions as the experimental set up. From the paper by Wang et al. [18], the ionic conductivity of the 80 μm thick membrane is 1.87 S m^{-1}.

However, they did not report the exchange current densities used in their work. For MEAs with a Nafion® membrane, much investigation has been conducted into the factors affecting the electrode activity, thus, the exchange current density is well-established. Such investigation has not yet been conducted for the PBI membrane/Pt catalyst interface. This value depends on a number of factors including the manufacturing and assembling techniques used to form the MEA. Since the exchange current density has not been reported, in our model, we adjust the cathode exchange current density to best fit the experimental data.

It is found that an exchange current density of 4×10^{-10} A m^{-2} at the cathode and 6 A m^{-2} at the anode give the best fit. Thus, these values will be used as the reference exchange current densities at 423 K and 1 atm. Fig. 2 shows the fit between the model predictions and the experimental polarization data.

Table 2
Membrane and diffuser properties

Membrane	
Thermal conductivity, k_m [26] (W m^{-1} K^{-1})	40
Ionic conductivity, σ_m [18] (S m^{-1})	1.87
Thickness, l_m [18] (m)	8×10^{-5}
Diffuser (graphite)	
Thermal conductivity, k_d (W m^{-1} K^{-1})	1.15
Electrical conductivity, σ_d (S m^{-1})	120
Porosity, ε	0.4
Particle diameter, d (m)	1.2×10^{-4}
Permeability, k_p (m^2)	1.8×10^{-11}
Thickness, l_d (m)	2.6×10^{-4}

Table 3
Catalyst layer properties

	Anode	Cathode
Reference exchange current density, i_0^{ref} (A m^{-2})	6	4×10^{-10}
Effective catalyst surface area, a (m^{-1})	1.4×10^{7}	5.6×10^{7}
Transfer coefficient, α	0.5	2
Concentration parameter, γ	0.5	1
Pt mass loading, m_{Pt} [18] (kg m^{-2})	0.005	0.02
Weight fraction of Pt in Pt/C, f	0.3	0.63
Porosity, ε	0.106	0.092
Permeability, k_p (m^2)	1.2×10^{-14}	5.5×10^{-15}
Reference pressure, P_{ref} (Pa)	1.013×10^{5}	1.013×10^{5}
Pt density, ρ_{Pt} (kg m^{-3})	21400	21400
C density, ρ_C (kg m^{-3})	1800	1800
Fraction of membrane phase in catalyst layer, $\varepsilon_{m,c}$	0.4	0.4
Catalyst layer thickness, l_c (m)	5×10^{-5}	5×10^{-5}
Pt particles diameter, d_{Pt} (m)	2×10^{-9}	2×10^{-9}

Table 4
Fluid properties [27,28]

	Oxygen	Water vapor	Hydrogen
Molar mass, M (kg mol^{-1})	32×10^{-3}	18×10^{-3}	2×10^{-3}
Thermal conductivity, k (W m^{-1} K^{-1})	0.0363	0.03	0.239
Heat capacity, c (J kg^{-1} K^{-1})	956	1980	14450
Kinematic viscosity, ν (m^2 s^{-1})	32.9×10^{-6}	31.11×10^{-6}	302×10^{-6}
Thermal diffusivity, α (m^2 s^{-1})	44.4×10^{-6}	30.8×10^{-6}	217×10^{-6}
Gas pair diffusivity, D_{mf} (m^2 s^{-1})	42.0×10^{-6}		144.0×10^{-6}

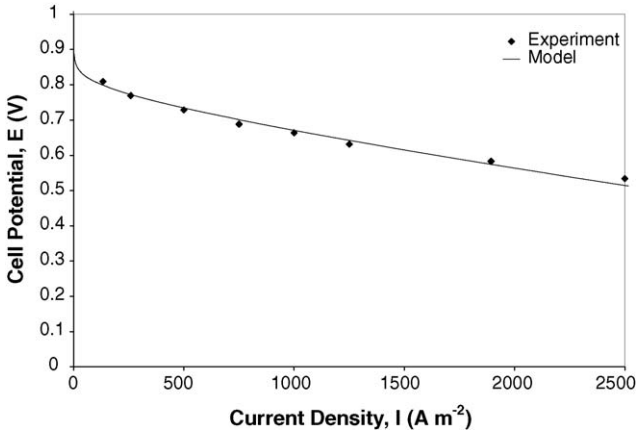

Fig. 2. Experimental and model polarization data.

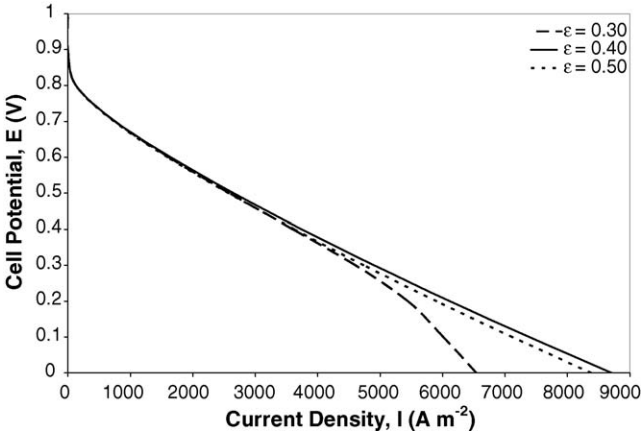

Fig. 4. Effect of gas diffuser porosity on polarization performance.

Fig. 3 shows the potential variation within the cell at limiting conditions for the base case. It shows a 0.372 V ohmic overpotential across the membrane and a 0.485 V activation overpotential ($\varphi_e - \varphi_s$) at the cathode. The former is due to low membrane conductivity while the latter is due to slow electrode kinetics at the cathode. The ohmic potential drop across the diffuser region is much lower (0.090 V total) due to its higher conductivity than the membrane. There is also a 0.194 V ohmic potential drop across the catalyst region since this region has a very low effective ionic conductivity.

To observe the effect of porous media characteristics on the fuel cell performance, four factors are varied—the gas diffuser porosity (ε^d), the anode f value (f_a), $a_{i0,ref}$ at the cathode, and the membrane conductivity (σ_m). Fig. 4 shows the effect of varying the gas diffuser porosity from its base value. Although the variation in performance is very small, the fuel cell performs better for a gas diffuser porosity of 0.4 than for 0.3 and 0.5. This suggests that for a given set of operating and geometric conditions, there exists an optimum gas diffuser porosity. The reason for this is a duality between effective conductivity and permeability as the porosity changes. Higher porosity implies higher permeability and thus, better flow of reacting gases. However, higher porosity means less solid region, hence, lower effective thermal and electrical conductivities. Thus, there will be larger ohmic potential drops, greater heat generation and higher temperature gradients. So, there is an optimum porosity, which gives the best balance between the two.

The IV curve for $\varepsilon = 0.3$ is the only one, where a distinct concentration overpotential region is seen. Since there is no liquid water, there is no blocking of the gas pores hence reduced transport limitation. However, the catalyst porosity depends on the gas diffuser porosity, and as porosity decreases, it becomes increasingly difficult for the gases to permeate the catalyst regions. When the gas diffuser porosity drops to 0.3 with the catalyst loading unaffected, the anode and cathode catalyst layer porosities drop to 0.05 and 0.03, respectively (Eq. (26)). Thus, it is not surprising that mass limitation becomes increasingly significant as porosity decreases.

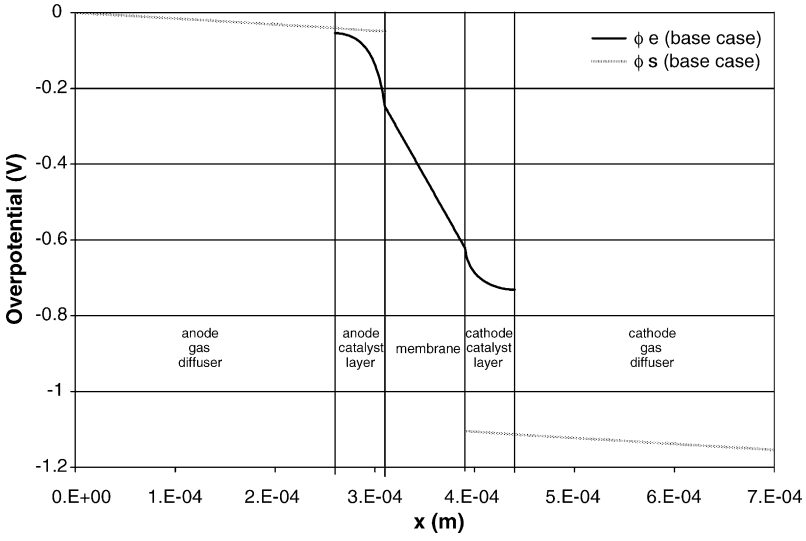

Fig. 3. Overpotentials at limiting conditions for the base case.

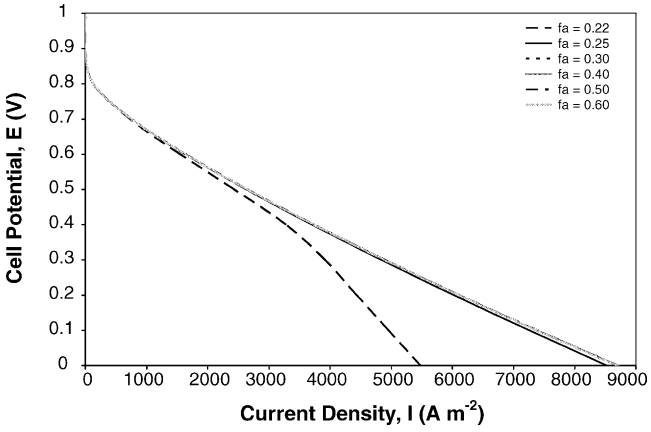

Fig. 5. Effect of Pt weight fraction of polarization performance.

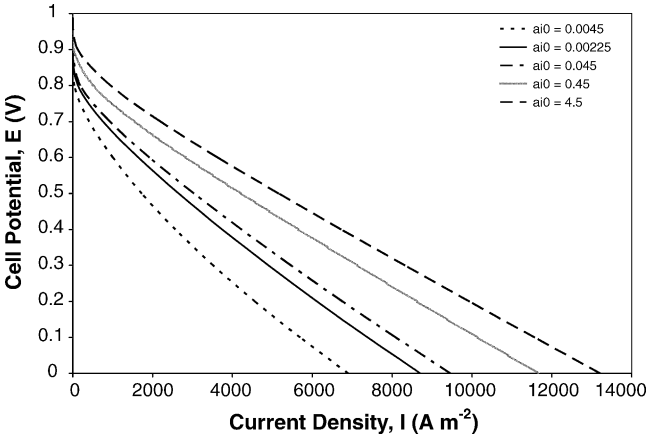

Fig. 7. Effect of cathode catalyst activity on polarization performance.

Fig. 5 shows the effect of varying f_a. Increasing f means that the carbon content in Pt/C is reduced while the Pt loading remains unaltered. This results in a less packed (more porous) but equally active catalyst region. Note that according to Eq. (28), varying f_a has a corresponding effect on f_c. It must be noted though that a certain amount of carbon is required to house the Pt particles; so, f cannot approach unity. Nevertheless the IV curves are barely distinguishable for f_a varying from 0.25 to 0.6. However, for $f_a = 0.22$, there is a sharp drop in IV performance. The reason for this is that for the base case condition ($f_a = 0.30$), the catalyst regions are not heavily packed ($\varepsilon \approx 0.1$). As f_a decreases, the catalyst layer porosity becomes lower hence mass transport limitations become more significant.

For $f_a = 0.22$, the anode and cathode catalyst layer porosities are 0.04 and 0.02, respectively (Eq. (26)). This would explain the concentration overpotential region in the IV curve for $f_a = 0.22$. Fig. 6 shows the oxygen concentration for $f_a = 0.22$ and 0.30 at limiting conditions ($E_{cell} = 0$). The fact that the mass fraction quickly drops to zero for $f_a = 0.22$ suggests that oxygen is not able to permeate the entire catalyst region, resulting in mass limitation effects and implying inefficient catalyst utilization. As f_a increases, the porosity of the catalyst layer increases, hence it becomes more permeable to the flow of reactant gases. As long as the catalyst porosity is not very close to zero, the fuel cell performs independently of f.

Fig. 7 shows the IV curves for different values of $a_{i0,ref}$. This value can be improved either by increasing the effective Pt surface area or by increasing the exchange current density. The latter can be achieved by better manufacturing and assembling methods, which ensure better physical and chemical contact between participating phases in the catalyst region. Predictably, the fuel cell performance increases significantly as the catalyst activity increases. The limiting current approximately doubles as $a_{i0,ref}$ increases from 0.0045

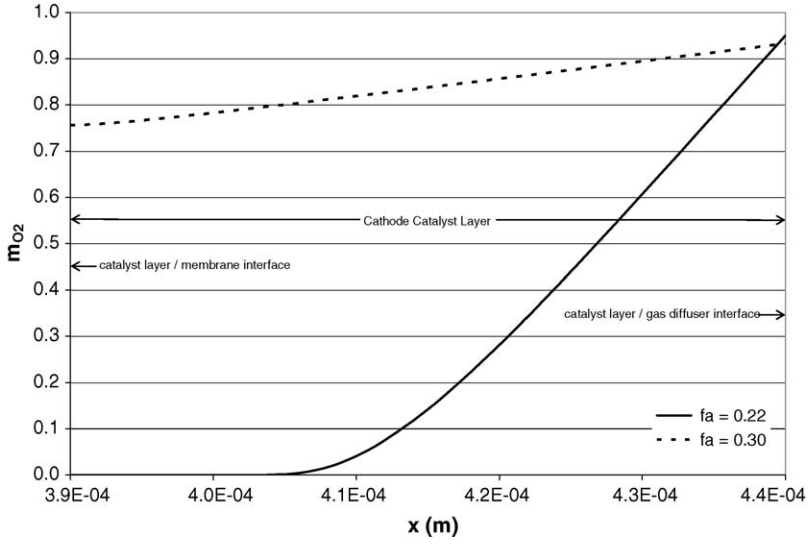

Fig. 6. Oxygen concentration across the catalyst layer at limiting conditions.

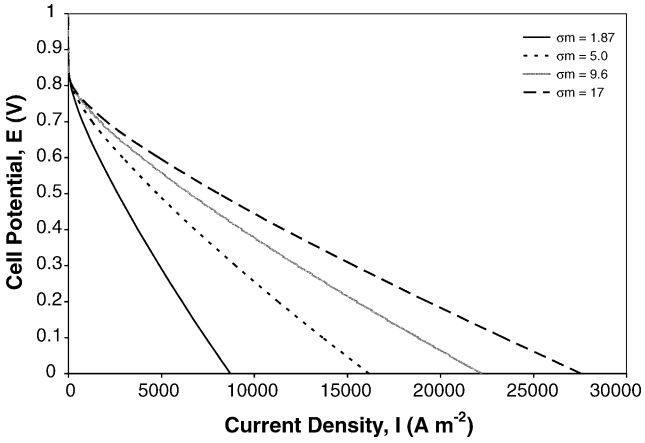

Fig. 8. Effect of membrane conductivity on polarization performance.

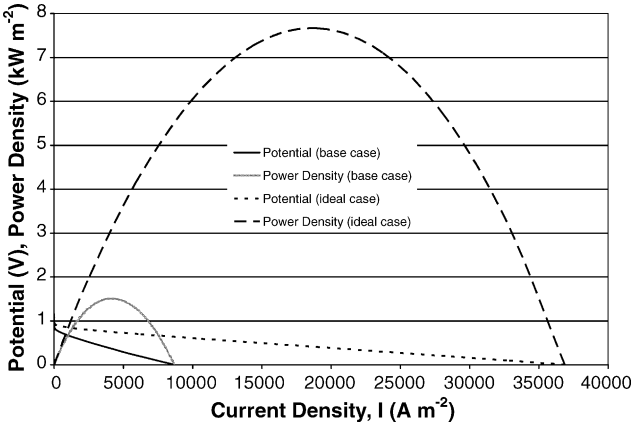

Fig. 9. Polarization and power density for the base case and ideal case.

to 4.5 A m^{-3}. Note that this is not an unrealistic improvement given that the corresponding value for an MEA using a Nafion® membrane is 500 A m^{-3} [29].

Fig. 8 shows the effect of increasing the membrane conductivity. The IV curves show a drastic improvement as the ionic conductivity approaches that of Nafion®. The value of 9.6 S m^{-1} is the maximum ionic conductivity reported for a composite of PBI in the literature. The ionic conductivity of Nafion® is 17 S m^{-1}.

So, Figs. 7 and 8 show that there is tremendous potential for improvement in PBIFC performance by increasing the membrane conductivity and enhancing the catalyst activity. Based on the above results, an ideal performance can be conceptualized for a PBIFC. Consider and MEA with catalyst particles containing 60 wt.% Pt/C, $a_{i0,ref} = 4.5$ A m^{-3} (the highest value in Fig. 7), $\sigma_m = 9.6$ S m^{-1} (the highest PBI membrane conductivity in the literature). All other operating conditions are the same. For these conditions, the optimum gas diffuser porosity is 0.3. This represents the ideal case.

Fig. 9 compares the base case performance with the ideal performance. There is a four-fold increase in limiting current density and a five-fold increase in peak power density. The peak power densities for the base case and ideal case are, respectively, 1.50 and 7.66 kW m^{-2}.The peak power density for the ideal case is in the same order as that of a Nafion® fuel cell. A major advantage with the intermediate temperature fuel cell is the absence of any distinguishable concentration overpotential region in the IV curve, implying that a high power density is sustainable over a wide range of current densities. With no need for water input into the fuel cell, and sustained power over a wide range of loading conditions, this makes the PBIFC very attractive for automotive applications.

Fig. 10 compares the temperature distribution across the MEA for the ideal case and the base case. For both cases, the temperature profile is selected at the point of optimum power

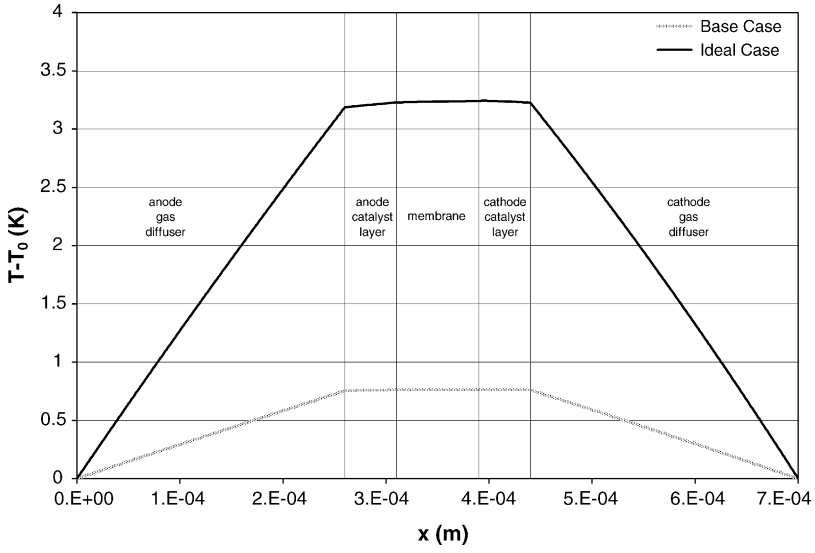

Fig. 10. Temperature distribution at optimum power density for the base case and ideal case.

(i.e. at a cell voltage of 0.4 V for both cases). The ideal case shows a maximum temperature rise of 3.2 K compared with 0.8 K for the base case. The reason for this difference is that for the ideal case, the current density is much higher resulting in greater ohmic heating and heat of reaction. For the ideal case at limiting conditions, the maximum temperature rise in the cell is 9 K (not shown). The typical temperature rise for a Nafion® fuel cell is 2–3 K [30–32]. However, heat removal is not as critical for PBI as it is for Nafion®. PBI is already more stable at higher temperatures, but most importantly, there is no danger of dehydration of the PBI membrane since it does not require liquid water.

4. Conclusions

A mathematical model of a PBIFC was developed with predicts the polarization characteristics as well as the one-dimensional transport phenomena across the MEA. Model results compare well with experimental data. Parametric studies into the porous media characteristics of the fuel cell show that the fuel cell performance is good as long as the catalyst regions are sufficiently porous. Mass limitation effects are only present when the catalyst regions are heavily packed, resulting in extremely low permeability to reactant flow.

The model results also predict that substantial improvements in fuel cell performance are possible as the conductivity of the PBI membrane and the cathode catalyst activity increase. Research is needed to better understand the interfacing between the PBI membrane and the Pt catalyst, and to find ways to make the catalyst more active. There exists great scope for research into finding composites of PBI whose conductivity approach that of Nafion®, as well as developing techniques to better apply the catalyst loading and assemble the MEA. The right combination of the above may prove to be a significant breakthrough in making fuel cell technology commercially viable.

Acknowledgements

The authors are grateful for the FIU Graduate School Dissertation Fellowship and to Gas Technology Institute (Contract Number 8390) for their support of this work.

References

[1] K.D. Kreuer, A. Fuchs, M. Ise, M. Spaeth, J. Maier, Imidazole and pyrazole-based proton conducting polymers and liquids, Electrochem. Acta 43 (1998) 1281–1288.
[2] R. Bouchet, E. Siebert, Proton conduction in acid doped polybenzimidazole, Solid State Ionics 118 (1999) 287–299.
[3] R. Bouchet, S. Miller, M. Duclot, J.L. Souquet, A thermodynamic approach to proton conductivity in acid-doped polybenzimidazole, Solid State Ionics 145 (2001) 69–78.
[4] O. Savadogo, Emerging membranes for electrochemical systems. Part II: high temperatures composite membranes for polymer electrolyte fuel cell (PEFC) applications, J. Power Sources 127 (2004) 135–161.
[5] C. Hasiotis, V. Deimede, C. Kontoyannis, New polymer electrolytes based on blends of sulfonated polysulfones with polybenzimidazole, Electrochim. Acta 46 (2001) 2401–2406.
[6] R. He, Q. Li, G. Xiao, N.J. Bjerrum, Proton conductivity of phosphoric acid doped polybenzimidazole and its composites with inorganic proton conductors, J. Membr. Sci. 226 (2003) 169–184.
[7] J.A. Asensio, S. Borros, P. Gomez-Romero, Enhanced conductivity in polyanion-containing polybenzimidazoles. Improved materials for proton-exchange membranes and PEM fuel cells, Electrochem. Commun. 5 (2003) 967–972.
[8] A. Schechter, R.F. Savinell, Imidazole and 1-methyl imidazole in phosphoric acid doped polybenzimidazole electrolyte for fuel cells, Solid State Ionics 147 (2002) 181–187.
[9] P. Staiti, M. Minutoli, Influence of composition and acid treatment on proton conduction of composite polybenzimidazole membranes, J. Power Sources 94 (2001) 9–13.
[10] J.S. Wainright, J.T. Wang, D. Weng, R.F. Savinell, M. Litt, Acid-doped polybenzimidazoles: a new polymer electrolyte, J. Electrochem. Soc. 142 (1995) 121.
[11] J.J. Fontanella, M.C. Wintersgill, J.S. Wainright, R.F. Savinell, M. Litt, High pressure electrical conductivity studies of acid doped polybenzimidazole, Electrochim. Acta 43 (1998) 1289–1294.
[12] Q. Li, H.A. Hjuler, N.J. Bjerrum, Phosphoric acid doped polybenzimidazole membranes: physiochemical characterization and fuel cell applications, J. Appl. Electrochem. 31 (2001) 773–779.
[13] B. Xing, O. Savadogo, Hydrogen/oxygen polymer electrolyte membrane fuel cells (PEMFCs) based on alkaline-doped polybenzimidazole (PBI), Electrochem. Commun. 2 (2000) 697–702.
[14] B. Xing, O. Savadogo, Hydrogen/oxygen polymer electrolyte membrane fuel cell (PEMFC) based on acid-doped polybenzimidazole (PBI), J. New Mater. Electrochem. Syst. 3 (2000) 345–349.
[15] D.M. Bernardi, M.W. Verbrugge, Mathematical model of a gas diffusion electrode bonded to a polymer electrolyte, AIChE J. 37 (1991) 1151–1163.
[16] D.M. Bernardi, M.W. Verbrugge, A mathematical model of the solid–polymer–electrolyte fuel cell, J. Electrochem. Soc. 139 (1992) 2477–2491.
[17] D. Cheddie, N. Munroe, Review and comparison of approaches to PEMFC modeling, J. Power Sources, in press.
[18] J.T. Wang, R.F. Savinell, J.S. Wainright, M. Litt, H. Yu, A H_2/O_2 fuel cell using acid doped polybenzimidazole as polymer electrolyte, Electrochim. Acta 41 (1996) 193–197.
[19] M. Kaviany, Principles of Heat Transfer in Porous Media, Springer-Verlag, NY, 1991.
[20] H. Rumpf, A.R. Gupte, Einfusse und korngrossenverteilung, in widerstandsdesetz der porenstromung, Chem.-Ing. Tech. 43 (1971) 367–375.
[21] G.R. Hadley, Thermal conductivity of packed metal powders, Int. J. Heat Mass Transfer 29 (1986) 909–920.
[22] D.L. Koch, J.F. Brady, Dispersion in fixed beds, J. Fluid Mech. 154 (1985) 399–427.
[23] G.H. Neale, W.K. Nader, Prediction of transport processes within porous media: diffusive flow processes within homogeneous swarm of spherical particles, AIChE J. 19 (1973) 112–119.
[24] R.E. Meredith, C.W. Tobias, Conduction in heterogeneous systems, in: C.W. Tobias (Ed.), Advances in Electrochemistry and Electrochemical Engineering, vol. 2, Interscience Publishers, NY, 1962.
[25] J.O. Robles, J.R. Regalbuto, The Engineering of Pt/Carbon Catalyst Preparation, Special Project, University of Illinois, Chicago, 2004.
[26] Boedeker Plastics Inc., Celazole® PolyBenzImidazole Specifications, URL: http://www.boedeker.com/celazo_p.htm.
[27] K. Wark, K. Wark Jr., Advanced Thermodynamics for Engineers, McGraw-Hill, NY, 1994.

[28] J.R. Welty, C.E. Wicks, R.E. Wilson, Fundamentals of Momentum, Heat and Mass Transfer, Wiley, NY, 1969.
[29] T. Zhou, H. Liu, A general three-dimensional model for proton exchange membrane fuel cells, Int. J. Transport Phenom. 3 (2001) 177–198.
[30] T. Berning, D.M. Lu, N. Djilali, Three-dimensional computational analysis of transport phenomena in a PEM fuel cell, J. Power Sources 106 (2002) 284–294.
[31] T. Berning, N. Djilali, Three-dimensional computational analysis of transport phenomena in a PEM fuel cell—a parametric study, J. Power Sources 124 (2003) 440–452.
[32] W.M. Yan, F. Chen, H.Y. Wu, C.Y. Soong, H.S. Chu, Analysis of thermal and water management with temperature-dependent diffusion effects in membrane of proton exchange membrane fuel cells, J. Power Sources 129 (2004) 127–137.